

Vortex Robot Platform for Autonomous Inspection: Modeling and Simulation

Angelica Brusell
Computer Science, Electrical and
Space Engineering
Luleå University of Technology
Luleå, Sweden
angbru@ltu.se

Georgios Andrikopoulos
Computer Science, Electrical and
Space Engineering
Luleå University of Technology
Luleå, Sweden
geoand@ltu.se

George Nikolakopoulos
Computer Science, Electrical and
Space Engineering
Luleå University of Technology
Luleå, Sweden
geonik@ltu.se

Abstract— In this article, the analytical modeling of a Vortex Robotic Platform (VRP) is investigated. Following the design of the Vortex Actuation (VA) unit and VRP presented in authors' previous work, the target goal is focused on providing a modeling methodology to include system dependencies on surfaces of different curvatures and robot orientations. The critical force model for guaranteeing successful adhesion is extracted for each case, while an overview of the maximum payload is also provided. The validity of the proposed methodology is evaluated through comparative simulations.

Keywords—Vortex Actuation, Adhesion Modeling, Climbing Robots, Inspection Robotics

I. INTRODUCTION

Climbing Robots (CRs) targeting inspection and maintenance tasks have been traditionally multidimensional in terms of utilized adhesion technologies and motion capabilities [1] while being tailored to match specific application scenarios, environments, surface materials and geometries [2]. Efficient handling of tools and sensors for Non-Destructive Testing (NDT) and Repair (NDR) tasks requires high payload capabilities, resulting in high adhesion requirements achieved by powerful actuators [3].

In Electric Ducted Fan (EDF) and generally rotor-based Wall Climbing Robot (WCR) literature, the main research aspect focuses on the analysis of negative pressure generation [4], generated thrust [5], [6], [7] general experimental studies [8] or design approaches targeting the maximization of the adhesion performance [9], [10]. Recent work provided novel considerations on the utilized hardware and software of the EDF-based CRs [11], [12], although no information was provided on adhesion modeling and control. Evaluation of these solutions was mostly performed on flat surfaces (e.g. wall, ceiling), while the analyzed adhesion was constrained on that particular single-plane case [9]. In [13], force and torque models were provided for a rotor-based CR in both flat and curved surfaces, although no input was provided on closed-loop force control or the cabling effects.

The novelty of the presented work stems from the formulation of an analytical force and torque model, with respect to the generalized case of the VRP [14], [15] being immobilized or moving on surfaces of variable inclinations and curvatures, while being analyzed through the challenging state where the robot's Center of Mass (CM) is misaligned from the geometrical center and at a variable position. The proposed methodology provides analytical models describing the critical adhesion force needed for ensuring successful operation in cases of variable orientation and surface curvature properties, while giving a detailed insight on the

payload capabilities of such robot designs. The presented analysis provides a theoretical framework for synthesizing energy-efficient adhesion controllers; an important step in the work towards untethered climbing robotics for inspection.

The rest of this article is structured as follows. Section II presents the details concerning the VRP prototype and its main components. Section III presents the VRP modeling approaches, from the scope of a force and torque analysis. Section IV provides the derivation of the critical adhesion force for successful attachment and immobilization, as well as the robot's maximum payload capability. Section V presents the numerical evaluation of the presented adhesion and payload models on flat and cylindrical surfaces. Finally, the concluding remarks are provided in Section VI.

II. VORTEX ROBOT PROTOTYPE

The VRP prototype, depicted in Fig. 1 [15], was designed with the primary goal of maximizing the payload that the robot can handle by utilizing a vortex actuator for achieving adhesion, while incorporating a differential-based design for enhancing the steering capabilities on various inclinations.

Specifically, the EDF is located in the middle of the robotic structure and it is supported from a ring-like frame. The EDF shroud is custom-designed and 3D printed for increasing the vortex generation, with dimensions chosen after an iterative sequence of design optimization for given robot dimensions and requirements posed from a set target application, as reported in [14]. The resulting configuration incorporated in the VRP prototype lead to a maximum adhesion force of approximately 8 kg [15]. Larger forces can be achieved for the same EDF power, by following the aforementioned methodology regarding shroud size and distance from surface, but at a cost of robot specifications.

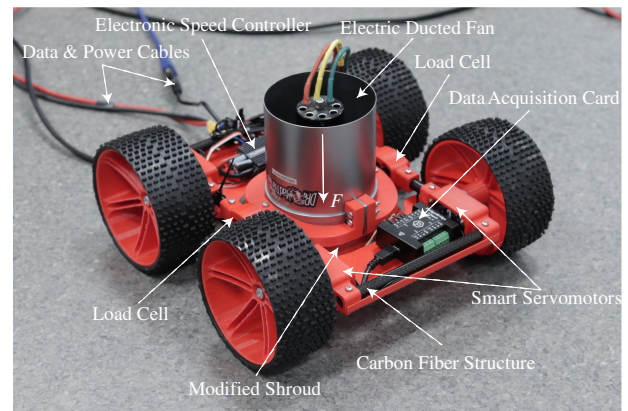


Fig. 1. The VRP prototype with highlighted components.

The frame supporting the EDF is connected on the vehicle via carbon fiber tubes that end in a casing for two load cells, which measure the total adhesion force. Locomotion is achieved via four smart servomotors mounted in a differential drive configuration. The overall VRP enclosure is 3D printed following the required design properties, leading to a prototype with mass $m = 2.11$ kg and dimensions of $0.27 \times 0.28 \times 0.15$ m (L×W×H).

III. FORCE AND TORQUE ANALYSIS

The main geometrical quantities of the VRP and their mathematical notations are presented in Fig. 2, which displays graphical representations of the platform in front, side and isometric views. The platform's position and orientation is defined by the local coordination system $G = \{O, x, y, z\}$ and angles $\{\varphi, \theta, \psi\} = \{\text{roll, pitch, yaw}\}$, with respect to the global coordination system $G_G = \{O_G, x_G, y_G, z_G\}$. Four points of rotation A_i , for $i = \{1, \dots, 4\}$, denote the geometrical centers of the four VRP wheels, which while rotating under ω_i velocity produce a robot linear velocity v and a robot heading δ as defined with respect to the y_0 axis of the initial local coordinate frame $G_0 = \{O_0, x_0, y_0, z_0\}$.

The generalized case of the VRP being in contact with a surface of unknown geometry is described by four random contact points B_i , defined as the geometrical centers of the

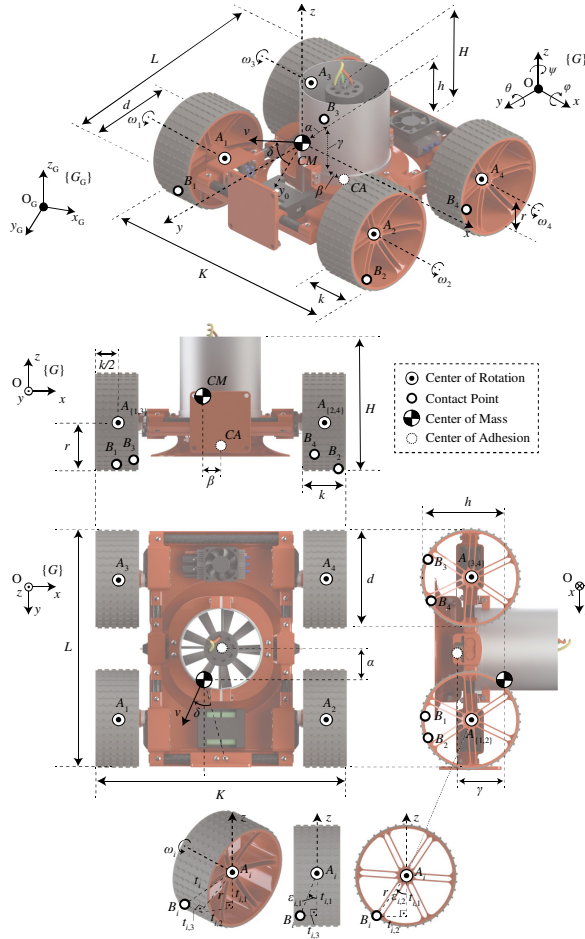


Fig. 2. Definition of the geometrical quantities utilized for the VRP's analysis, under the generic case of contact with a surface of random geometry, highlighted by the randomly defined wheel contact center points.

contact surfaces for each wheel. A single wheel analysis, as shown in Fig. 2 under front side and isometric views, is providing the definition of the contact point distance t_i to the wheel center of rotation and its projections $t_{i,j}$ for $j = \{1, 2, 3\}$ on the z axis of the robot coordination system.

A variable Center-of-Mass (CM) is defined under a three-axis displacement defined by the distances α, β and γ from the point of adhesion CA. In this case, the CA point is defined, with the assumption of a uniform generation of adhesion, as coincident both to the longitudinal axis of the VA motor and the plane of rotation of the ESC blades. In addition, K, L , and H of the VRP define the width, length and height, respectively, d, r and k are the respective diameter, radius and width of the wheels, while h is the maximum, in the direction of the z axis, distance of the CM to the wheel outer surface.

Under all surface cases, the main forces acting on the VRP are the weight W , originating at CM, the adhesion force F_{VA} originating at CA and coincident to the longitudinal axes of the EDF motor, the motion forces $F_{w,i}$ generated by each wheel motor, the reaction forces N_i and the respective friction forces T_i , all originating at the wheel contact points B_i ($i = \{1, \dots, 4\}$). The torques applied on the VRP include the wheel motor torques τ_i with direction defined by the respective rotational velocities ω_i , as well as the internal torques generated by the acted forces on the wheels and CM.

- *Successful adhesion performance* is defined as rotational equilibrium, i.e. zero sum of torques τ , in the x and y axes $\sum \tau_x = \sum \tau_y = 0$, and equilibrium of forces in the z direction $\sum F_z = 0$.
- *robot immobilization* is defined as both translational $\sum F_n = 0$ and rotational $\sum \tau_n = 0$ equilibrium in all three axes ($n = \{x, y, z\}$), with zero linear velocity $v = 0$.

A. Flat Surfaces

The force diagram of the VRP placed on a flat surface of arbitrary dimensions is presented in Fig. 3. While placed on the test plane, defined by the $\{x_s, y_s\}$ axes of the system $G_s = \{O_s, x_s, y_s, z_s\}$, the acting forces are analysed for the two subcases of an horizontal surface (Fig. 3 (top)), where the $\{x_s, y_s\}$ plane is coincident to the $\{x_G, y_G\}$, and the generalized case where the surface is rotated by angles $\{\varphi_s, \theta_s, \psi_s\}$ around the $\{x_s, y_s, z_s\}$ axes (Fig. 3 (bottom)). Rotational equilibrium for ensuring successful adhesion yields $\{\varphi, \theta\} = \{\varphi_s, \theta_s\}$, while the case of robot immobilization and rotational equilibrium gives $\{\varphi, \theta, \psi\} = \{\varphi_s, \theta_s, \psi_s\}$. Surface rotation around an x - y - z sequence leads to the derived weight W coefficients:

$$W_x = mg (s\varphi s\psi + c\varphi c\psi s\theta) \quad (1)$$

$$W_y = mg (c\psi s\varphi - c\varphi s\psi s\theta) \quad (2)$$

$$W_z = mg c\varphi c\theta \quad (3)$$

with the resulting static forces described by:

$$\sum F_x = -\sum_{i=1}^4 T_{i,x} + W_x = ma_{v,x} \quad (4)$$

$$\sum F_y = \sum_{i=1}^4 F_{w,i} - \sum_{i=1}^4 T_{i,y} + W_y = ma_{v,y} \quad (5)$$

$$\sum F_z = \sum_{i=1}^4 N_i - W_z - F_{VA} = 0 \quad (6)$$

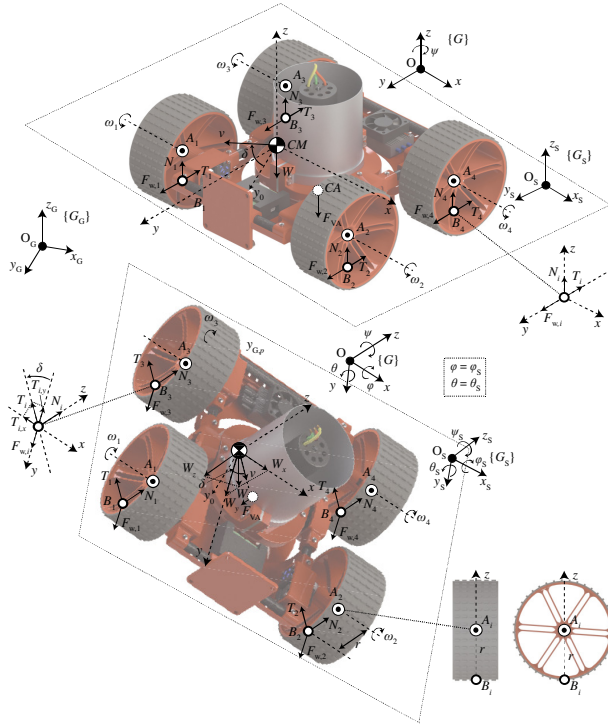


Fig. 3. Force diagram for the VRP while on a flat surface under (top) horizontal and (bottom) random inclination

where $c\cdot$ and $s\cdot$ denote the trigonometric functions $\cos(\cdot)$ and $\sin(\cdot)$, respectively, while a_v denotes the vehicle acceleration being analysed to its two $a_{v,x} = a_v s\delta$ and $a_{v,y} = a_v c\delta$ coefficients across the x and y axes. The torque analysis with respect to CM and around the three local axes becomes:

$$\sum \tau_x = -h \sum_{i=1}^4 F_{w,i} + h \sum_{i=1}^4 T_{i,y} + (L/2 - r + \alpha)(N_3 + N_4) - (L/2 - r - \alpha)(N_1 + N_2) + \alpha F_{VA} = 0 \quad (7)$$

$$\sum \tau_y = -h \sum_{i=1}^4 T_{i,x} + ((K - k)/2 + \beta)(N_2 + N_4) - ((K - k)/2 - \beta)(N_1 + N_3) - \beta F_{VA} = 0 \quad (8)$$

$$\sum \tau_z = ((K - k)/2 + \beta)(-F_{w,2} - F_{w,4} + T_{2,y} + T_{4,y}) - ((K - k)/2 - \beta)(-F_{w,1} - F_{w,3} + T_{1,y} + T_{3,y}) + (L/2 - r + \alpha)(T_{3,x} + T_{4,x}) - (L/2 - r - \alpha)(T_{1,x} + T_{2,x}) = I\alpha_z \quad (9)$$

where I is the moment of inertia and α_z the rotational acceleration around z axis.

B. Curved Surfaces

The below analysis has been focused on the VRP moving along: *i*) the circumference of a cylindrical surface with radius R , defined by $\psi = 0^\circ$ and $\theta = 0^\circ$ (Fig. 4), and *ii*) its longitudinal axis i.e. $\psi = 90^\circ$ and $\theta = 0^\circ$ (Fig. 5).

1) $\psi = 0^\circ$: The forces acting on the VRP while moving along the circumference of the surface G_s is presented in detail in Fig. 4.

The motion forces $F_{w,i}$, adhesion force F_{VA} , weight vector W , reaction forces N_i and generated wheel frictions T_i are analyzed to their coefficients on the $\{y, z\}$ plane, via utilization of the angles $\varphi_{\{1,2,3\}}$ as $\varphi_1 = \angle \langle x_s, B_{\{3,4\}} \rangle \langle x_s, CM \rangle$, $\varphi_2 = \angle \langle x_s, CM \rangle \langle x_s, CA \rangle$, and $\varphi_3 = \angle \langle x_s, CM \rangle \langle x_s, B_{\{1,2\}} \rangle$,

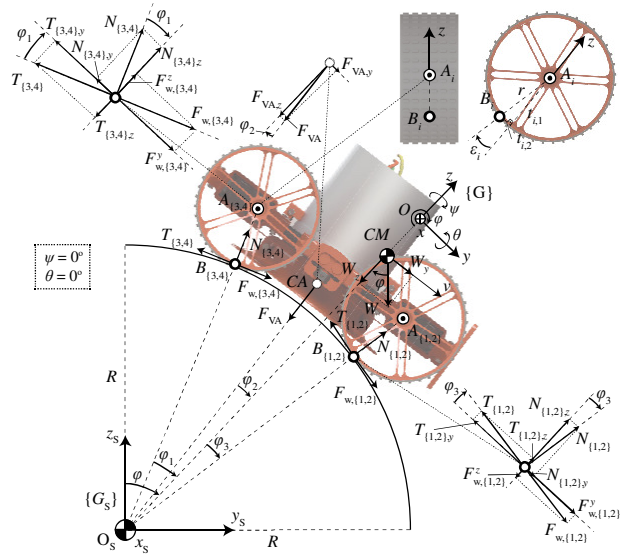


Fig. 4. Force diagram for the VRP while moving on a cylindrical surface and under orientation $\psi = \theta = 0^\circ$.

while the overall symmetry of the robot yields $\varphi_1 - \varphi_2 = \varphi_2 + \varphi_3$. Finally, the contact points B_i and wheel center A_i lie on coincident lines, $\overline{x_s A_i} \equiv \overline{x_s B_i}$, hence the angles $\{\varphi_1, \varphi_2, \varphi_3\}$ can be calculated as $\varphi_1 = \tan^{-1}((L - 2(r - \alpha))/(2R))$, $\varphi_2 = \tan^{-1}(\alpha/R)$ and $\varphi_3 = \tan^{-1}((L - 2(r + \alpha))/(2R))$.

The static force equations describing the VRP moving on a cylindrical surface under $\psi = 0^\circ$ and $\theta = 0^\circ$ are the following:

$$\sum F_x = 0, \quad (10)$$

$$\sum F_y = \sum_{i=1}^4 F_{w,i}^y - \sum_{i=1}^4 T_{i,y} + N_{1,y} + N_{2,y} - N_{3,y} - N_{4,y} + F_{VA,y} + W_y = ma_v, \quad (11)$$

$$\sum F_z = -F_{w,1}^z - F_{w,2}^z + F_{w,3}^z + F_{w,4}^z + T_{1,z} + T_{2,z} - T_{3,z} - T_{4,z} + \sum_{i=1}^4 N_{i,z} - F_{VA,z} - W_z = 0 \quad (12)$$

A single wheel analysis under front and side views, is providing the projected distances t_{ij} for $j = \{1, 2\}$ on the z axis. Due to the curved target surface, the contact points B_i have an offset $t_{\{1,2\},2} = rs\varphi_3$ and $t_{\{3,4\},2} = rs\varphi_1$ from the center of the wheel as depicted in Fig. 4. Taking this into account, the following torque analysis is formulated:

$$\begin{aligned} \sum \tau_x = & (L/2 - r - t_{\{1,2\},2} - \alpha)(-F_{w,1}^z - F_{w,2}^z + T_{1,z} + T_{2,z} + N_{1,z} + N_{2,z})\chi \\ & + (h - (r - t_{\{1,2\},1})) (F_{w,1}^y + F_{w,2}^y - T_{1,y} - T_{2,y} + N_{1,y} + N_{2,y}) \\ & + (L/2 - r - t_{\{3,4\},2} + \alpha)(-F_{w,3}^z - F_{w,4}^z + T_{3,z} + T_{4,z} - N_{3,z} - N_{4,z}) \quad (13) \\ & - (h - (r - t_{\{3,4\},1})) (-F_{w,3}^y - F_{w,4}^y + T_{3,y} + T_{4,y} + N_{3,y} + N_{4,y}) \\ & + \gamma F_{VA,y} + \alpha F_{VA,z} = 0 \end{aligned}$$

$$\begin{aligned} \sum \tau_y = & ((K - k)/2 - \beta)(-F_{w,3}^z + F_{w,1}^z + T_{3,z} - T_{1,z} - N_{3,z} - N_{1,z}) \\ & + ((K - k)/2 + \beta)(-F_{w,2}^z + F_{w,4}^z + T_{2,z} - T_{4,z} + N_{2,z} + N_{4,z}) - \beta F_{VA,z} = 0 \quad (14) \end{aligned}$$

$$\begin{aligned} \sum \tau_z = & ((K - k)/2 - \beta)(F_{w,1}^y + F_{w,3}^y - T_{1,y} - T_{3,y} + N_{1,y} - N_{3,y}) \\ & - ((K - k)/2 + \beta)(-F_{w,4}^y - F_{w,2}^y + T_{4,y} + T_{2,y} + N_{4,y} - N_{2,y}) + \beta F_{VA,y} = 0 \quad (15) \end{aligned}$$

As seen in (12), (13)–(15), the sum of all forces in the z directions and sum of all torques in all three directions have

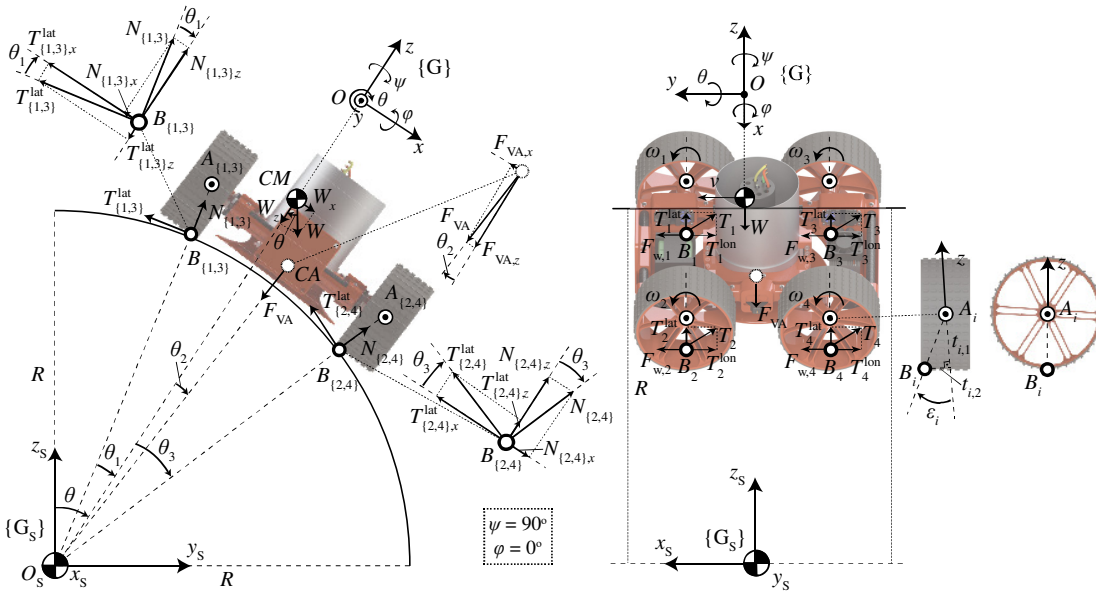


Fig. 5. Force diagram for the VRP moving on a cylindrical surface and under orientation $\psi = 90^\circ$ and $\phi = 0^\circ$.

been equated to zero, for satisfying the kinematic requirements posed by the definition of successful adhesion and the linear motion defined by $\psi = 0^\circ$.

2) $\psi = 90^\circ$: The forces acting on VRP while moving along the longitudinal axis of the cylindrical surface with frame $G_S = \{O_S, x_S, y_S, z_S\}$ is presented in Fig. 5.

In this case, $\{x_S, z_S\}$ coincidence is valid for the points of rotation A_i and contact points B_i of the left $i = \{1, 3\}$ and right sides $i = \{2, 4\}$ of the robot. The dominant angle of rotation is θ and is utilized for the analysis of the weight vector W in its two coefficients W_y and W_z . In addition, the direction of linear motion that is coincident to the y axis and the acting weight coefficient W_x have a direct effect on the direction of the friction vectors T_i , which are analyzed to their longitudinal T_i^{lon} and lateral T_i^{lat} coefficients. The former coefficients react to the linear motion across the surface's longitudinal axis, while the latter react to the effect of the W_x and the potential undesired sliding along the x axis.

The adhesion force F_{VA} , reaction forces N_i , weight vector W and generated lateral wheel frictions T_i^{lat} are analysed to their coefficients on the $\{x, z\}$ plane, via utilization of the geometrically analysed angles $\theta_{\{1,2,3\}}$ as $\theta_1 = \angle \langle x_S, B_{\{1,3\}} \rangle \langle x_S, CM \rangle$, $\theta_2 = \angle \langle x_S, CM \rangle \langle x_S, CA \rangle$, and $\theta_3 = \angle \langle x_S, CM \rangle \langle x_S, B_{\{2,4\}} \rangle$, while the overall symmetry of the robot yields $\theta_1 + \theta_2 = \theta_3 - \theta_2$. Finally, due to symmetry of the curved surface the contact point B_i and wheel center A_i lie on coincident lines, $\overline{x_S A_i} \equiv \overline{x_S B_i}$, hence the angles $\{\theta_1, \theta_2, \theta_3\}$ can be calculated as $\theta_1 = \tan^{-1}((W - w - 2\beta)/(2R))$, $\theta_2 = \tan^{-1}(\beta/R)$ and $\theta_3 = \tan^{-1}((W - w + 2\beta)/(2R))$.

The resulting static force equations describing the VRP moving on a cylindrical surface under $\psi = 90^\circ$ and $\phi = 0^\circ$ with absence of slippage along the x axis are the following:

$$\sum F_x = -\sum_{i=1}^4 T_{i,x}^{lat} + N_{2,x} + N_{4,x} - N_{1,x} - N_{3,x} - F_{VA,x} + W_x = 0, \quad (16)$$

$$\sum F_y = \sum_{i=1}^4 F_{w,i} - \sum_{i=1}^4 T_{i,y}^{lon} = m a_y, \quad (17)$$

$$\sum F_z = +T_{2,z}^{lat} + T_{4,z}^{lat} - T_{1,z}^{lat} - T_{3,z}^{lat} + \sum_{i=1}^4 N_{i,z} - F_{VA,z} - W_z = 0. \quad (18)$$

As shown in Fig. 5, the contact points B_i have an offset $t_{\{2,3\},2} = r \tan(\theta_3 - \theta_2)$ and $t_{\{1,3\},2} = r \tan(\theta_1)$ from the center of the wheel, which leads to the following torque analysis:

$$\sum \tau_x = -h \sum_{i=1}^4 F_{w,i} + h \sum_{i=1}^4 T_{i,y}^{lon} + (L/2 - r - \alpha)(T_{1,z}^{lat} - T_{2,z}^{lat} - N_{1,z} - N_{2,z}) + (L/2 - r + \alpha)(-T_{4,z}^{lat} + T_{3,z}^{lat} + N_{3,z} + N_{4,z}) + \alpha F_{VA,z} = 0 \quad (19)$$

$$\begin{aligned} \sum \tau_y = & ((K - k)/2 - t_{\{2,4\},2} + \beta)(T_{2,z}^{lat} + T_{4,z}^{lat} + N_{2,z} + N_{4,z}) \\ & + h(-T_{2,x}^{lat} - T_{4,x}^{lat} + N_{2,x} + N_{4,x}) \\ & + ((K - k)/2 - t_{\{1,3\},2} - \beta)(T_{1,z}^{lat} + T_{3,z}^{lat} - N_{1,z} - N_{3,z}) \\ & - h(T_{1,x}^{lat} + T_{3,x}^{lat} + N_{1,x} + N_{3,x}) - \gamma F_{VA,x} - \beta F_{VA,z} = 0 \end{aligned} \quad (20)$$

$$\begin{aligned} \sum \tau_z = & (L/2 - r - \alpha)(T_{3,x}^{lat} - T_{1,x}^{lat} + N_{3,x} - N_{1,x}) \\ & + (L/2 - r + \alpha)(T_{2,x}^{lat} - T_{4,x}^{lat} + N_{2,x} - N_{4,x}) \\ & + ((K - k)/2 - t_{\{2,4\},2} + \beta)(-F_{w,2} - F_{w,4} + T_{2,y}^{lon} + T_{4,y}^{lon}) \\ & + ((K - k)/2 - t_{\{1,3\},2} - \beta)(F_{w,1} + F_{w,3} - T_{1,y}^{lon} - T_{3,y}^{lon}) - \alpha F_{VA,x} = 0 \end{aligned} \quad (21)$$

IV. CRITICAL ADHESION FORCE MODELING

A. Theoretical Modeling

1) *Flat Surface*: The assumed translational equilibrium in the z axis (6) yields the reaction force $N = \sum_{i=1}^4 N_i = F_{VA} + W_z$, while friction T is defined as:

$$T = \sum_{i=1}^4 T_i = \mu \sum_{i=1}^4 N_i = \mu(F_{VA} + W_z), \quad (22)$$

where μ is the static friction constant. As shown in Fig. 3, the total friction T becomes equal to the vector addition of W_x and $F_w + W_y$, where $F_w = \sum_{i=1}^4 F_{w,i}$, thus by combining (3) and (22) the critical force $F_{VA} = F_c$ is computed:

$$F_c(\varphi, \theta, \psi, F_w, a_v) = \frac{1}{\mu} \sqrt{(mg s \varphi)^2 + (mg c \varphi s \theta)^2 + F_w^2 + 2mg F_w (c \psi s \varphi - c \varphi s \psi s \theta)} - \frac{ma_v}{\mu} - mg c \varphi c \theta \quad (23)$$

In the case of immobilization leading to translational equilibrium in the $\{x, y\}$ plane ($\sum F_{\{x, y\}} = 0$) and locked wheels, i.e. $F_w = 0$, the above model becomes:

$$F_{c,0} = \begin{cases} 0 & \text{for } 0 \leq \gamma \leq \gamma_c \\ mg \left(\sqrt{(s \varphi)^2 + (c \varphi s \theta)^2} / \mu - c \varphi c \theta \right) & \text{for } \gamma_c \leq \gamma \leq (360^\circ - \gamma_c) \\ 0 & \text{for } (360^\circ - \gamma_c) \leq \gamma \leq 360^\circ \end{cases} \quad (24)$$

which has to be constrained at the regions where the adhesion force becomes negative, which are defined by using the l^2 -norm (i.e. Euclidean norm) $\gamma = \sqrt{\varphi^2 + \theta^2}$ with critical value $\gamma_c = \varphi_c = \theta_c$. In addition, (24) reveals its independence of the “yaw”, ψ , and CM variations.

2) *Curved Surface* ($\psi = 0^\circ$): The assumed translational equilibrium in the z axis (12) yields the reaction force:

$$N = \frac{F_{VA} c \varphi_2 + mg c \varphi - 2F_w (s \varphi_1 - s \varphi_3)}{2(c \varphi_1 + c \varphi_3 + \mu s \varphi_1 - \mu s \varphi_3)} \quad (25)$$

while the resulting friction T is defined as:

$$T = \mu \sum_{i=1}^4 N_i = \mu \frac{F_{VA} c \varphi_2 + mg c \varphi - 2F_w (s \varphi_1 - s \varphi_3)}{2(c \varphi_1 + c \varphi_3 + \mu s \varphi_1 - \mu s \varphi_3)} \quad (26)$$

With no forces acting in the x axis, solving (11) using (25) yields the critical adhesion force F_c :

$$F_c(\varphi, F_w, a_v) = \frac{2F_w(Q_1 c \varphi_3 + Q_1 c \varphi_1 + Q_2 s \varphi_1 - Q_2 s \varphi_3)}{Q_2 c \varphi_2 - Q_1 s \varphi_2} + \frac{mg(Q_1 s \varphi - Q_2 c \varphi) - Q_1 ma_v}{Q_2 c \varphi_2 - Q_1 s \varphi_2} \quad (27)$$

where Q_1 and Q_2 are constants for a given CM displacement:

$$Q_1 = c \varphi_1 + c \varphi_3 + \mu s \varphi_1 - \mu s \varphi_3, \quad Q_2 = s \varphi_1 - s \varphi_3 + \mu c \varphi_1 + \mu c \varphi_3. \quad (28)$$

Thus, in the case of robot immobilization ($a_v=0$) and $F_w=0$, the critical force becomes:

$$F_{c,0} = \begin{cases} 0 & \text{for } 0 \leq \varphi \leq \varphi_c \\ \frac{mg(Q_1 s \varphi - Q_2 c \varphi)}{Q_2 c \varphi_2 - Q_1 s \varphi_2} & \text{for } \varphi_c \leq \varphi \leq (360^\circ - \varphi_c) \\ 0 & \text{for } (360^\circ - \varphi_c) \leq \varphi \leq 360^\circ \end{cases} \quad (29)$$

where φ_c denotes the critical slippage angle.

3) *Curved Surface* ($\psi = 90^\circ$): The assumed translational equilibrium in the z axis (18) yields the reaction force:

$$N = \frac{F_{VA} c \theta_2 + mg c \theta}{2(c \theta_1 + c \theta_3 + \mu s \theta_3 - \mu s \theta_1)} \quad (30)$$

In order to enforce $\psi = 90^\circ$ as well as no slippage, the sum of lateral forces in x axis described by (16) has to be zero, so the lateral friction force in x can be stated as:

$$T^{\text{lat}} = 2N(s \theta_3 - s \theta_1) - F_{VA} s \theta_2 + mg s \theta. \quad (31)$$

Using (17) we get the frictional force in the longitudinal direction of motion:

$$T^{\text{lon}} = \sum_{i=1}^4 T_i^{\text{lon}} = \sum_{i=1}^4 F_{w,i} - ma_v, \quad (32)$$

Finally, the resulting friction T for the immobilized case is defined as:

$$T = \mu \sum_{i=1}^4 N_i = \mu \frac{F_{VA} c \theta_2 + mg c \theta}{2(c \theta_1 + c \theta_3 + \mu s \theta_3 - \mu s \theta_1)}. \quad (33)$$

Solving (33) using (32) yields the critical adhesion force F_c :

$$F_c(\theta, T) = \frac{2T(c \theta_1 + c \theta_3 + \mu s \theta_3 - \mu s \theta_1) - \mu mg c \theta}{\mu c \theta_2} \quad (34)$$

In the case of robot immobilization ($a_v=0$) and $F_w=0$, the critical adhesion force becomes:

$$F_{c,0} = \begin{cases} 0 & \text{for } 0 \leq \theta \leq \theta_c \\ \frac{mg(Q_3 s \theta - Q_4 c \theta)}{Q_4 c \theta_2 + Q_3 s \theta_2} & \text{for } \theta_c \leq \theta \leq (360^\circ - \theta_c) \\ 0 & \text{for } (360^\circ - \theta_c) \leq \theta \leq 360^\circ \end{cases} \quad (35)$$

where Q_3 and Q_4 are constants for a given CM displacement:

$$Q_3 = c \theta_1 + c \theta_3 + \mu s \theta_3 - \mu s \theta_1, \quad Q_4 = s \theta_1 - s \theta_3 + \mu c \theta_1 + \mu c \theta_3. \quad (36)$$

and θ_c denotes the critical slippage angle.

B. Payload Analysis

Considering the loaded VRP state as $m = m_0 + m_L$, where m_0 denotes the unloaded system's mass on the VRP, the presented geometrical models can provide an estimation of the payload m_L for a given critical force F_c :

1) *Flat Surface*: From the geometrical model (23), we receive the VRP payload description for a given F_w and a_v :

$$m_L(\varphi, \theta, \psi, F_w, F_{VA}, a_v) = \frac{-Q_5 \pm \sqrt{(Q_5)^2 - 2Q_6 \left(\left(\frac{F_w}{\mu} \right)^2 - F_{VA}^2 \right)}}{Q_6} - m_0, \quad (37)$$

where Q_5 and Q_6 are calculated via:

$$Q_5 = \frac{2g F_w (c \psi s \varphi - c \varphi s \psi s \theta)}{\mu^2}, \quad Q_6 = 2 \left(\frac{(g s \varphi)^2 + (g c \varphi s \theta)^2 - (\mu g c \varphi c \theta)^2 - (a_v)^2}{\mu^2} \right). \quad (38)$$

The sub-case of the immobilized robot becomes:

$$m_{L,0} = \begin{cases} m_{L,\max} & \text{for } 0 \leq \gamma \leq \gamma_{\text{crit}} \\ \frac{F_{VA}}{g \left(\frac{1}{\mu} \sqrt{(s \varphi)^2 + (c \varphi s \theta)^2} - c \varphi c \theta \right)} - m_0 & \text{for } \gamma_{\text{crit}} \leq \gamma \leq (360^\circ - \gamma_{\text{crit}}) \\ m_{L,\max} & \text{for } (360^\circ - \gamma_{\text{crit}}) \leq \gamma \leq 360^\circ \end{cases} \quad (39)$$

where $m_{L,\max}$ denotes the VRP's maximum structural load.

2) *Curved Surface* ($\psi = 0^\circ$): Using (26), the maximum payload can be calculated as:

$$m_L(\varphi, \theta, \psi, F_w, F_{VA}, a_v) = \frac{F_{VA} (Q_2 c \varphi_2 - Q_1 s \varphi_2) - 2F_w (Q_1 c \varphi_3 + Q_1 c \varphi_1 + Q_2 s \varphi_1 - Q_2 s \varphi_3)}{Q_1 g s \varphi - Q_2 g c \varphi - Q_1 a_v} - m_0 \quad (40)$$

For the immobilized case ($F_w = a_v = 0$) as described in (29), the maximum payload becomes:

$$m_{L,0} = \begin{cases} m_{L,\max} & \text{for } 0 \leq \varphi \leq \varphi_{\text{crit}} \\ \frac{F_{VA} (Q_2 c \varphi_2 - Q_1 s \varphi_2)}{Q_1 g s \varphi - Q_2 g c \varphi} - m_0 & \text{for } \varphi_{\text{crit}} \leq \varphi \leq (360^\circ - \varphi_{\text{crit}}) \\ m_{L,\max} & \text{for } (360^\circ - \varphi_{\text{crit}}) \leq \varphi \leq 360^\circ \end{cases} \quad (41)$$

3) *Curved Surface* ($\psi = 90^\circ$): Similarly, the maximum payload $m_L(\varphi, \theta, \psi, F_w, F_{VA}, a_v)$ is calculated from (33), while for the immobilized case described in (34) it becomes:

$$m_{L,0} = \begin{cases} m_{L,\max} & \text{for } 0 \leq \theta \leq \theta_{\text{crit}} \\ \frac{F_{VA}(Q_4 c \theta_2 + Q_3 s \theta_2)}{Q_3 g s \theta - Q_4 g c \theta} - m_0 & \text{for } \theta_{\text{crit}} \leq \theta \leq (360^\circ - \theta_{\text{crit}}) \\ m_{L,\max} & \text{for } (360^\circ - \theta_{\text{crit}}) \leq \theta \leq 360^\circ \end{cases} \quad (42)$$

C. Numerical Modeling

For the needs of the presented evaluation, Matlab's Simscape (Fig. 6) was used for computing the critical force under robot immobilization and locked wheels. The criteria of the VRP remaining immobilized on the surface, produced the minimum adhesion force required for all roll and pitch values, which defines a numerical model $F_{c,n}(\varphi, \theta)$ that is being used in the next Section for model comparison purposes.

V. SIMULATION RESULTS

The basic properties of the VRP prototype utilized in the following theoretical and numerical evaluations are $m = m_0 = 2.112$ kg, $\mu = 0.8$, $L = 0.272$ m, $W = 0.288$ m, $H = 0.150$ m, $r = 0.055$ m, $w = 0.055$ m, $g = 9.807$ m/s², $F_{VA,\max} = 80$ N, and $m_{L,\max} = 10$ kg. As the unloaded VRP prototype followed a symmetrical design approach, it led to negligible CM α and β distances from the CA, which for the needs of the performed simulations are assumed zero $\{\alpha, \beta\} \approx 0$, while the γ distance estimated at $\gamma = 15$ mm is not affecting the critical force and therefore is not incorporated. An exhaustive testing was performed for all three cases presented above, on *i*) a flat surface under (φ, θ) angle combinations from 0° to 360° , *ii*) a cylindrical surface of $R = 1$ m and $\psi = 0^\circ$ and under orientations φ from 0° to 360° , and *iii*) the same cylindrical surface with $\psi = 90^\circ$ and under orientations θ from 0° to 360° , while for all cases the adhesion forces was ranging from 0 to 80 N.

A. Flat Surfaces

Simulation of (24) for the aforementioned physical properties of the VRP prototype, led to the $F_{c,0}(\varphi, \theta)$ representation displayed in Fig. 7. From the view of a single angular change, the critical force presents a symmetrical response around the inverted surface case (point A), where it is equal to the robot's weight (20.7 N). The vertical surface cases (points B and C) require a larger force of approximately 25.9 N, while the maximum value of 33.5 N is reached at $\varphi = 129^\circ$ and 231° . It must be noted that angle values below 38.5° (point F) and over 321.5° (point G) denote the critical angles $\gamma_c = \varphi_c = \theta_c$. Also, the minimum force required to maintain adhesion for any surface orientation is revealed at 33.5 N.

The error $e_{F,c} = F_{c,n}(\varphi, \theta) - F_{c,0}(\varphi, \theta)$ between the theoretical and numerically extracted models is presented in Fig. 8. For all inclination combinations, the two models remain arithmetically close, with the difference reaching a mean of approximately 0.3 N and a maximum of 0.8 N, which highlights the validity of the theoretical analysis.

Finally, by setting the $F_{c,\max} = F_{VA,\max} = 80$ N, the simulation of (39) returns a static map of the maximum permitted payload $m_{L,0}$ (Fig. 9). As highlighted in Fig. 9, in the inverted case, described by $\varphi = 180^\circ$ and $\theta = 0^\circ$, the VRP's permitted payload reaches 6.05 kg, while in the most challenging case identified as $\varphi = 135^\circ$ and $\theta = 0^\circ$, the robot prototype could manage approx. 2.98 kg.

B. Curved Surfaces

For the unloaded VRP case, the robot's CM tends to the CA and therefore giving $\varphi_1 = \varphi_3$ and $\varphi_2 = 0$. Both the numerical

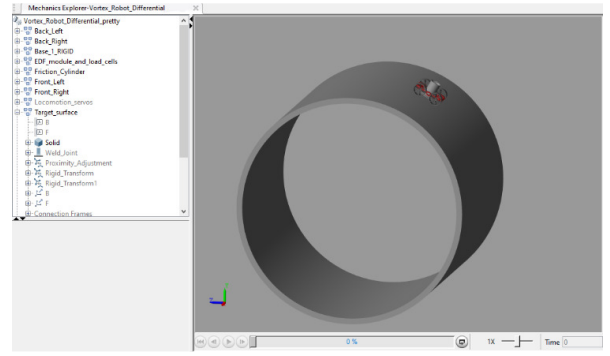


Fig. 6. Overview of the Simscape Mechanics Explorer displaying the simulated VRP dynamically moving on surfaces of variable curvatures.

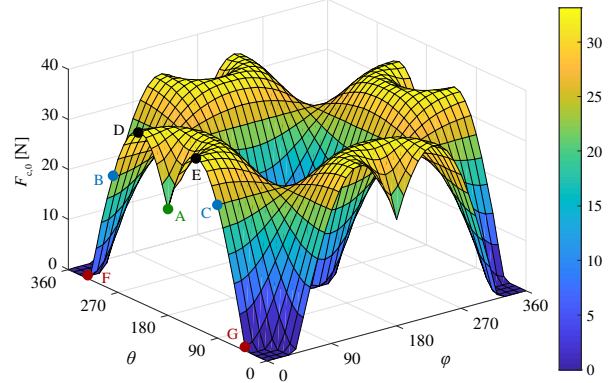


Fig. 7. Critical force (24) needed for successful adhesion of the VRP on a flat surface of varying roll and pitch inclinations.

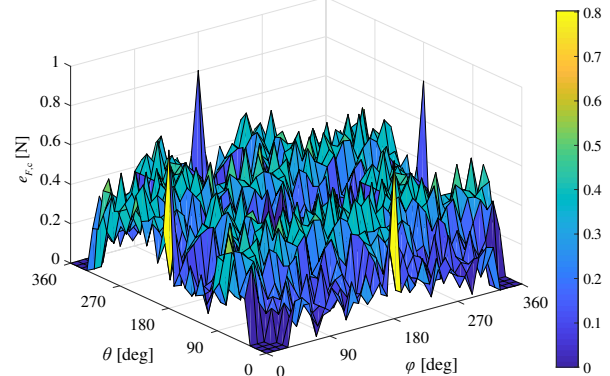


Fig. 8. Error between the theoretical (24) and the numerically extracted force model under different roll and pitch changes.

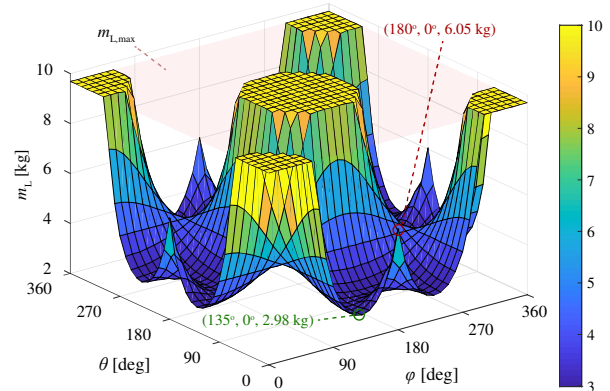


Fig. 9. Maximum permitted payload on a surface on a surface of varying roll and pitch inclinations.

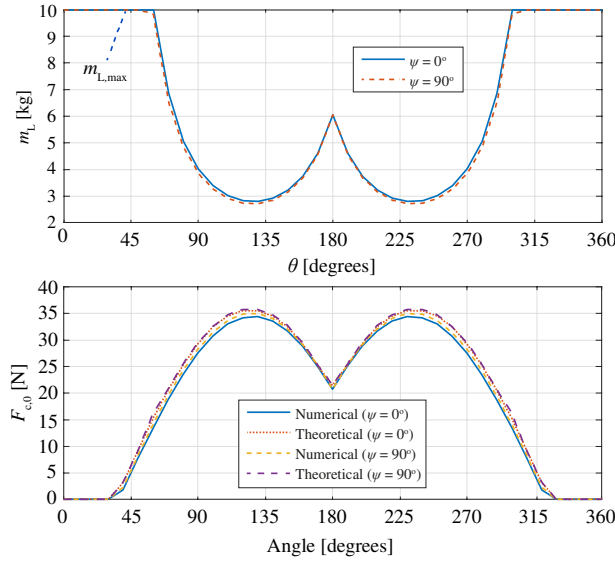


Fig. 10. (Top) Numerically evaluated critical adhesion force $F_{c,0}$ on a cylindrical surface for $\psi = 0^\circ$ and $\psi = 90^\circ$ robot orientations, while compared to the respective theoretical models (29) and (35). (Bottom) Maximum permitted payload m_L on a cylindrical surface under the two analyzed robot orientations ($\psi = 0^\circ$ and $\psi = 90^\circ$).

Simscape and theoretical adhesion force models for a) $\psi = 0^\circ$ and b) $\psi = 90^\circ$ were evaluated for φ and θ between 0° and 360° , respectively, with the results being shown in Fig. 10 (top).

All plotted models show a general increase in required adhesion forces in comparison to the flat surface results, while displaying an underestimation of critical force reaching a maximum difference of 1.3 N, when compared to their respective numerical values. The small documented difference between the two orientation cases is expected, given that the VRP design is characterized by a small difference in $\varphi_1 = \varphi_3 \approx 4.6^\circ$ and $\theta_1 = \theta_3 \approx 6.6^\circ$, respectively.

Finally, for the maximum adhesion force of the VRP prototype $F_{c,max} = F_{VA,max} = 80$ N, the simulation of (41) and (42) under the aforementioned physical quantities would return the maximum permitted payload $m_{L,0}$ for the two robot orientations on the curved surface. As highlighted in Fig. 10 (bottom), the maximum payload curves are providing similar results, with the payload reaching 6.05 kg for φ (θ) = 180° and the minimum values of 2.70 – 2.80 kg for φ (θ) = 125° and 235° . The latter is the maximum payload that guarantees adhesion under both analyzed orientations and for all φ and θ . The reason for the similar payload capabilities is again due to the small $\varphi_{1,3}$ and $\theta_{1,3}$, while the larger the cylinder's radii, the closer the force descriptions to the ones for the flat surface.

VI. CONCLUSIONS

In this article, a force and torque model of a Vortex Robotic Platform's (VRP's) was formulated and evaluated. An analytical model representation was provided, with respect to the generalized case of the VRP being immobilized or moving on flat and curved surfaces. Focus was given on these particular surface cases, extracted as the dominant geometries found on general infrastructure (bridges, wind turbines, airplanes, pipe systems etc.) in need of frequent, accurate and fast inspection. The challenging state where the robot's Center of Mass (CM) is misaligned from its geometrical center was investigated, while providing the theoretical basis for

synthesizing models describing the critical adhesion force needed for ensuring adhesion regardless of robot orientation, surface curvature, attached payload and its positioning onto the robot's chassis. Further analysis was also provided on the maximum payload capabilities, resulting in a static map identifying the VRP's expected performance.

Finally, simulation trials were performed on the critical force methodology and maximum payload, while compared to numerically extracted models via dynamic simulations. For all investigated surface cases, the models were characterized by a close match and a slight underestimation in the case of the static analysis, which showed the potential of utilizing the presented theoretical framework in model-based controllers of climbing robots for Non-Destructive Testing (NDT) tasks.

REFERENCES

- [1] A. Brusell, G. Andrikopoulos, G. Nikolakopoulos, "A Survey on Pneumatic Wall-Climbing Robots for Inspection", in 24th Mediterranean Conference on Control and Automation (MED), 21–24 June 2016, Athens, Greece.
- [2] R. D. Dethe and S. B. Jaju, "Developments in Wall Climbing Robots : A Review," *Int. J. Eng. Res. Gen. Sci.*, vol. 2, no. 3, pp. 33–42, 2014.
- [3] M. Al Rashed et al., "Climbing Robots for NDT Applications," in *CLAWAR 2017: 20th International Conference on Climbing and Walking Robots and the Support Technologies for Mobile Machines*, 2017.
- [4] J. Xiao, A. Sadegh, M. Elliott, A. Calle, A. Persad, and H. M. Chiu, "Design of Mobile Robots with Wall Climbing Capability," *Proceedings, 2005 IEEE/ASME International Conference on Advanced Intelligent Mechatronics*, pp. 24–28, 2005.
- [5] J. Xiao, B. Li, K. Ushiroda, and Q. Song, "Rise-Rover: A Wall-Climbing Robot with High Reliability and Load-Carrying Capacity," *Proceedings of the 2015 IEEE Conference on Robotics and Biomimetics*, pp. 2072–2077, 2015.
- [6] P. Sekhar and R. Bhooshan, "Duct Fan Based Wall Climbing Robot for Concrete Surface Crack Inspection," *IEEE India Conference (INDICON)*, 2014.
- [7] P. J. Sanchez-Cuevas, G. Heredia, and A. Ollero, "Multirotor UAS for bridge inspection by contact using the ceiling effect," *2017 Int. Conf. Unmanned Aircr. Syst. ICUAS 2017*, pp. 767–774, 2017.
- [8] J. Zhao, X. Li, and J. Bai, "Experimental study of vortex suction unit-based wall-climbing robot on walls with various surface conditions," *Proc. Inst. Mech. Eng. Part C J. Mech. Eng. Sci.*, vol. 231, no. 21, pp. 3977–3991, 2018.
- [9] Q. Zhou and X. Li, "Design of Wall-climbing Robot Using Electrically Activated Rotational-flow Adsorption Unit," *2016 IEEE/RSJ International Conference on Intelligent Robots and Systems (IROS)*, pp. 5758–5763, 2016.
- [10] X. Li and L. Dong, "Development and Analysis of an Electrically Activated Sucker for Handling Workpieces with Rough and Uneven Surfaces," *IEEE/ASME Trans. Mechatronics*, vol. 21, no. 2, pp. 1024–1034, 2016.
- [11] B. Li, K. Ushiroda, L. Yang, Q. Song, and J. Xiao, "Wall-climbing robot for non-destructive evaluation using impact-echo and metric learning SVM," *Int. J. Intell. Robot. Appl.*, vol. 1, no. 3, pp. 255–270, 2017.
- [12] L. Yang et al., "Wall-climbing robot for visual and GPR inspection," *Proc. 13th IEEE Conf. Ind. Electron. Appl. ICIEA 2018*, pp. 1004–1009, 2018.
- [13] M. G. Alkalla, M. A. Fanni, A. M. Mohamed, and S. Hashimoto, "Tele-operated propeller-type climbing robot for inspection of petrochemical vessels," *Ind. Robot An Int. J.*, vol. 44, no. 2, pp. 166–177, 2017.
- [14] G. Andrikopoulos, and G. Nikolakopoulos, "Vortex Actuation via Electric Ducted Fans: An Experimental Study", in *Springer's Journal of Intelligent & Robotic Systems*, July, 2018.
- [15] A. Papadimitriou, G. Andrikopoulos, G. Nikolakopoulos, "Development and Control of a Differential Wall Climbing Robot based on Vortex Adhesion", in *European Control Conference (ECC)*, 25-28 June 2019, Naples, Italy.